

# ON GRID-INDEPENDENCE OF RANS PREDICTIONS FOR AERODYNAMIC FLOWS USING MODEL-CONSISTENT UNIVERSAL WALL-FUNCTIONS

**T. Knopp**

\*DLR (German Aerospace Center), Institute of Aerodynamics and Flow Technology  
Bunsenstr. 10, 37073 Göttingen, Germany  
e-mail: [Tobias.Knopp@dlr.de](mailto:Tobias.Knopp@dlr.de)

**Key words:** Wall function, RANS turbulence modelling, boundary layer approximation, separation

**Abstract.** *A universal wall-function method for RANS turbulence modelling is presented, which is designed by consistency between the global turbulence model and the near-wall model. This ensures solutions independent of the wall-distance of the first grid node above the wall provided it is located in the logarithmic part of the boundary layer or below. The near-wall RANS solutions of the Spalart-Allmaras and SST  $k-\omega$  turbulence model are investigated in regions of strong adverse pressure gradient leading to separation, and suggestions for the design of wall-function methods for non-equilibrium flows are given. New universal wall-functions in closed-form are proposed, which give almost grid-independent predictions for equilibrium boundary layers for all variants of the Spalart-Allmaras and the  $k-\omega$  model resp. The method is then applied successfully to aerodynamic flows with separation including a transonic flow with shock induced separation and a subsonic highlift airfoil close to stall.*

## 1 INTRODUCTION

This paper is dedicated to *turbulence-model consistent universal wall-functions* for aerodynamic flows with separation. This method allows for a considerable solver acceleration and reduction of memory consumptions at only a small loss in accuracy even in flows with separation and reattachment. The huge computing costs for 3D flow simulations in complex geometries are still a major limiting factor in the "appropriate" usage (in terms of the numerical discretization error) of CFD tools in industry, in particular for unsteady calculations. An additional need for acceleration arises as CFD-solvers are more and more used as part of optimization processes, which requires fast CFD-solutions for a large number of geometrical configurations without loss in accuracy.

Denote  $y^+(1) = y(1)u_\tau/\nu$  the distance of the first node above the wall in viscous length-scales where  $y(1)$  is the wall distance,  $u_\tau$  is the friction velocity and  $\nu$  is the viscosity. The aim of hybrid wall functions is to provide a boundary condition for solid walls that enables flow solutions

independent of the location of the first grid node above the wall, allowing large values of  $y^+(1)$  in regions of attached flow. Classical *low-Re boundary conditions* impose no-slip at the wall and the RANS equations are integrated down to the wall, which requires a so-called *low-Reynolds grid* with  $y^+(1) \approx 1$ . Then up to 50% of the boundary-layer nodes reside in the near-wall region. Moreover, this increases the numerical stiffness due to the small cell height in conjunction with the steep gradients. *High-Re boundary conditions* use the standard wall-function formulation and prescribe the wall-shear stress and no-penetration at the wall. The RANS equations are solved only down to the inner part of the logarithmic layer and are matched with the logarithmic law of the wall at the first grid node above the wall. High-Re boundary conditions require a so-called *high-Reynolds grid* with  $y^+(1) \gtrsim 40$  being located in the log-layer. Moreover we introduce the term *intermediate-Re grid* to refer to the buffer layer, which is the region between viscous sublayer and log-layer.

Despite their strong relevance in CFD and the more than thirty years enduring efforts in this topic, the applicability of most wall-function approaches e.g. [4, 5, 6, 7] is limited, since grid-independent solutions cannot be obtained for flows with separation.

The major short-coming of standard wall-functions is that the underlying high-Re grid requirement ceases to be valid inevitably in flows with separation. The grid generator usually produces a grid with an almost constant  $y(1)$ -distribution over the body surface. Then in regions of attached equilibrium flow, the corresponding distribution of  $y^+(1)$  is also nearly constant and the high-Re constraint can be satisfied. But as the separation point is approached,  $y^+(1)$  goes to zero as friction velocity is zero at separation. Then two situations have to be distinguished. Firstly, there are flows with an abrupt violation of the high-Re condition, e.g. shock-induced separation in transonic flows or geometry-induced separation due to a backward facing step. Secondly, there are flows with a continuously increasing violation when separation is caused by a smooth adverse pressure gradient, e.g. for an airfoil or blade close to stall. Moreover, in recirculation regions,  $y^+(1)$  is much smaller than in regions of attached flow, and the high-Re condition is also violated.

Historically, the first improvement over standard wall-functions was to use a so-called *hybrid* formulation, see e.g. [4, 5] which removes the high-Re grid constraint in a natural way. Other approaches to remedy the high-Re grid constraint by [6, 8] will be discussed below. Hybrid wall-functions are approximative velocity profiles for the entire near-wall region down to the wall. In turbulent boundary layer flows close to equilibrium, they give grid-independent solutions on high-Re grids (similar to standard wall-functions). On low-Re and intermediate-Re grids, results in  $c_f$  deviate by at most 10%-15% from the low-Re solution but these predictions are dependent on the location where matching of outer flow and wall-function occurs. The grid-dependent spreading is caused by an inconsistent coupling of two different eddy-viscosity models, viz., a one- resp. two-equation model for the global (outer) flow and an algebraic model (e.g. the model by Spalding [13] in [4]) in the near-wall region (wall-function).

This grid-dependence is the reason for poor predictions of flows with separation. An initially high-Re grid with  $y^+(1) \approx 50$  remote from the separation point becomes more and more a low-Re grid when approaching separation. Each change in  $y^+(1)$  gives a small modelling error,

which is accumulated and thus may lead to poor predictions near separation and reattachment. Hence the second crucial modification was to devise universal wall-functions which are consistent with the turbulence model of the global (outer) flow, as revealed first by [1]. Such wall-functions are based on the universality of the near-wall RANS solutions for each given one- resp. two-equation model in zero-pressure gradient (ZPG) turbulent boundary layer flows. In [1], consistency is achieved by using a spline interpolation of the near-wall RANS solution for a ZPG boundary layer. The criterion of model-consistency ensures results independent of the location of the matching node (except numerical errors), see [1, 2].

Application to aerodynamic flows requires further investigation. Such flows include stagnation points and subsequent not fully developed turbulent flow, regions of strong pressure gradient with a large pressure gradient parameter  $p^+ = \nu/(\rho u_\tau^3) dp/dx$  due to the typically moderate Reynolds number, and regions of separated flow. An investigation of the range of validity of model-consistent wall-functions in such flow situations and a discussion of the treatment of the turbulence variables in wall-function methods is given in [3].

This paper is organized as follows. Section 2 gives the governing equations for compressible fluid flow and RANS turbulence modelling. In Section 3 the proposed wall-function method is described and validated for a flat plate turbulent boundary layer at ZPG. The role of the pressure gradient parameter is discussed in Section 4. The numerical method is described in Section 5. In Section 6 the method is applied to aerodynamic flows with separation. A discussion vis a vis the work of [7, 8] is included in Section 7.

## 2 RANS EQUATIONS FOR TURBULENT COMPRESSIBLE FLOWS

We consider the steady-state Favre-averaged compressible Navier-Stokes equations in a bounded Lipschitz domain  $\Omega \subset \mathbb{R}^d$  ( $d = 2, 3$ ). We use the eddy-viscosity assumption for the Reynolds-stress tensor and the gradient-diffusion approximation for the turbulent heat-flux vector. We seek velocity  $\vec{u}$ , density  $\rho$ , pressure  $p$ , and temperature  $\theta$  s.t.

$$\vec{\nabla} \cdot (\rho \vec{u}) = 0 \quad \text{in } \Omega, \quad (1)$$

$$\vec{\nabla} \cdot (\rho \vec{u} \otimes \vec{u}) - \vec{\nabla} \cdot [2\mu_e \mathbb{T}(\vec{u})] + \vec{\nabla} p = 0 \quad \text{in } \Omega, \quad (2)$$

$$\vec{\nabla} \cdot (\rho \vec{u} H) - \vec{\nabla} \cdot [\vec{u} (2\mu_e \mathbb{T}(\vec{u}))] - \vec{\nabla} \cdot (\kappa_e \vec{\nabla} \theta) = 0 \quad \text{in } \Omega \quad (3)$$

We use the Sutherland law for molecular viscosity  $\mu$  and the equations of state  $p = \rho R \theta$ ,  $e = c_v \theta$  for specific internal energy, and  $h = e + p/\rho = c_p \theta$  for specific enthalpy, with gas constant  $R$ , specific heat at constant volume  $c_v$ , specific heat at constant pressure  $c_p$ . Denote  $H = h + \frac{1}{2} \vec{u} \cdot \vec{u}$  the total enthalpy and  $\mathbb{T}(\vec{u})$  and moreover we define the strain rate tensor

$$\mathbb{T}(\vec{u}) \equiv \mathbb{S}(\vec{u}) - \frac{1}{3} \vec{\nabla} \cdot \vec{u} \mathbb{I}, \quad \text{with} \quad \mathbb{S}(\vec{u}) = \frac{1}{2} \left( \vec{\nabla} \vec{u} + (\vec{\nabla} \vec{u})^T \right),$$

effective viscosity  $\mu_e = \mu + \mu_t$  and effective thermal conductivity  $\kappa_e = \kappa + \kappa_t$  where  $\kappa = c_p \mu / Pr$ ,  $\kappa_t = c_p \mu_t / Pr_t$  with laminar and turbulent Prandtl numbers  $Pr = 0.72$  and  $Pr_t = 0.85$

resp.

The Spalart-Allmaras type one-equation turbulence models [9, 10] compute the eddy viscosity  $\mu_t$  from the relation  $\mu_t = \rho\nu_t$  with  $\nu_t = f_{v1} \max(\tilde{\nu}; 0)$  where  $\tilde{\nu}$  is the solution of the transport equation

$$\vec{\nabla} \cdot (\rho\vec{u}\tilde{\nu}) - \vec{\nabla} \cdot \left( \frac{\mu + \rho\tilde{\nu}}{\sigma} \vec{\nabla}\tilde{\nu} \right) - \rho \frac{c_{b2}}{\sigma} (\vec{\nabla}\tilde{\nu}) \cdot (\vec{\nabla}\tilde{\nu}) = c_{b1}\rho\tilde{S}\tilde{\nu} - c_{w1}\rho f_w \left( \frac{\tilde{\nu}}{d} \right)^2$$

with  $d$  being the distance to the closest wall and near-wall damping function  $f_{v1} = \chi^3/(\chi^3 + c_{v1}^3)$  with  $\chi = \tilde{\nu}/\nu$ . On walls  $\tilde{\nu} = 0$  is prescribed.

Several  $k$ - $\omega$  model versions (e.g. [11], [19], [20], [21]) have evolved from the original proposal [12] where  $\mu_t = \rho k/\omega$  and  $k, \omega$  are the solution of

$$\begin{aligned} \vec{\nabla} \cdot (\rho\vec{u}k) - \vec{\nabla} \cdot \left( (\mu + \sigma_k\mu_t) \vec{\nabla}k \right) &= 2\mu_t \mathbb{T}(\vec{u}) : \vec{\nabla}\vec{u} - \beta_k \rho k \omega \\ \vec{\nabla} \cdot (\rho\vec{u}\omega) - \vec{\nabla} \cdot \left( (\mu + \sigma_\omega\mu_t) \vec{\nabla}\omega \right) &= 2\gamma\rho \mathbb{T}(\vec{u}) : \vec{\nabla}\vec{u} - \beta_\omega \rho \omega^2 \end{aligned}$$

with constants  $\beta_k, \beta_\omega, \gamma, \sigma_k$  and  $\sigma_\omega$ . We impose  $k = 0$  on solid walls.

Regarding  $\omega$ , asymptotic theory (cf. [12]) gives the near-wall behaviour  $\omega = 6\nu/(\beta_\omega y^2)$  which becomes singular at the wall. In industrial RANS solvers, the boundary condition Equation (26) in [11] (abbreviated Menter b.c.) is very popular. Alternatively, Wilcox [12] suggests to prescribe  $\omega$  at the first grid point above the wall  $\Gamma_\delta$  at wall-distance  $y_\delta$  located in the viscous sublayer (Wilcox b.c.):

$$\text{Menter b.c.: } \omega = C_w \omega_\delta \quad \text{on } \Gamma_w, \quad \text{with } \omega_\delta = \frac{6\nu}{\beta_\omega y_\delta^2}, \quad C_w = 10 \quad (4)$$

$$\text{Wilcox b.c.: } \omega = \omega_\delta \quad \text{on } \Gamma_\delta, \quad \text{with } \omega_\delta = \frac{6\nu}{\beta_\omega y_\delta^2}. \quad (5)$$

### 3 TURBULENCE MODEL CONSISTENCY OF UNIVERSAL WALL FUNCTIONS

The aim of wall-functions is to remedy the no-slip boundary condition for (2) and the required near-wall resolution of the RANS solution (For (3) an adiabatic wall is assumed).

#### 3.1 Wall function formulation

For this purpose, we couple the global RANS problem solved in the entire computational domain  $\Omega$  with a problem to be solved in the near-wall region  $\Omega_\delta$  via a domain-decomposition with full overlap as sketched in Figure 1, see [14, 3]. For this purpose let  $\Gamma_\delta$  denote the artificial inner boundary located within or below the logarithmic part of the boundary layer.

1. *Global RANS problem.* Solve the full compressible RANS plus turbulence model equations in the whole domain  $\Omega$  with modified wall boundary condition for momentum, where the wall-shear stress is prescribed instead of imposing no-slip:

$$\vec{u} \cdot \vec{n} = 0, \quad (\mathbb{I} - \vec{n} \otimes \vec{n}) 2\mu_e \mathbb{T}(\vec{u}) \vec{n} = -\tau_w^{\text{bl}} \vec{u}_t \quad \text{on } \Gamma_w \quad (6)$$

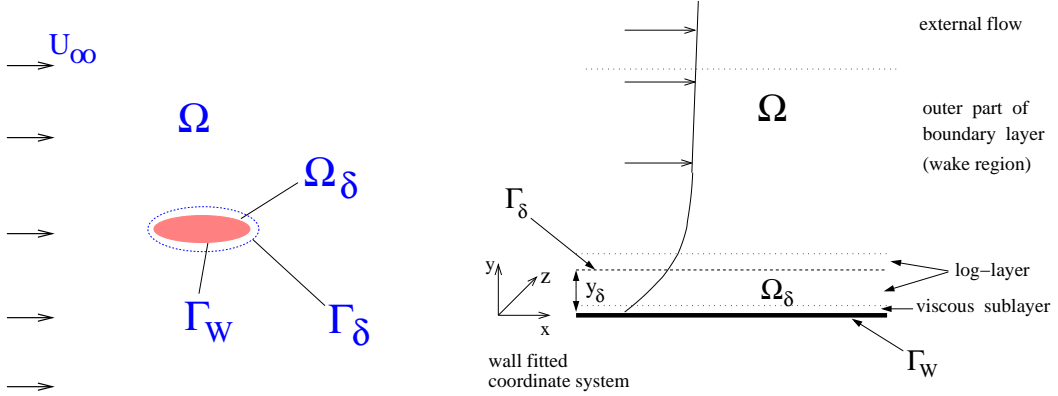


Figure 1: Domain decomposition with full overlap in the near-wall region.

Therein,  $\mathbb{I} - \vec{n} \otimes \vec{n}$  is the projection operator onto the tangential space of  $\Gamma_w$  and  $\vec{u}_t$  denotes the unit velocity vector in streamwise direction

$$\vec{u}_t = \frac{\vec{v}_t}{|\vec{v}_t|}, \quad \vec{v}_t = (\mathbb{I} - \vec{n} \otimes \vec{n})\vec{u}|_{\Gamma_\delta} \quad \text{with} \quad (\mathbb{I} - \vec{n} \otimes \vec{n})_{ij} = \delta_{ij} - n_i n_j \quad (7)$$

with  $\delta_{ij} = 1$  if  $i = j$  and zero otherwise ( $1 \leq i, j \leq d$ ).

2. *Near-wall RANS problem.* Solve the full compressible RANS plus turbulence model equations in the near-wall region  $\Omega_\delta$  with no-slip condition at the wall and matching of global flow and near-wall problem at the inner matching boundary  $\Gamma_\delta$

$$\vec{u}^{\text{bl}} = \vec{0} \quad \text{on} \quad \Gamma_w, \quad \vec{u}^{\text{bl}} = \vec{u} \quad \text{on} \quad \Gamma_\delta. \quad (8)$$

3. *Compute wall shear stress.* The wall shear stress  $\tau_w^{\text{bl}}$  is determined from the near-wall solution  $\vec{u}^{\text{bl}}$  via

$$(\mathbb{I} - \vec{n} \otimes \vec{n})2\mu_e^{\text{bl}}\mathbb{T}(\vec{u}^{\text{bl}})\vec{n} = -\tau_w^{\text{bl}}\vec{u}_t \quad \text{on} \quad \Gamma_w \quad (9)$$

### 3.2 Boundary-layer approximation for universal wall functions

The idea of the wall-function method is to compute  $\tau_w$  from the solution of a simplified set of equations called boundary layer equations. Firstly, numerical tests show that effects of compressibility in the near-wall region are negligible for Mach numbers smaller 1.4. Secondly, the near-wall attached flow is already surprisingly well described by the one-dimensional boundary layer equations, except very close to flow separation and reattachment, where a two-dimensional boundary layer model is superior.

Then, for each  $\vec{x}_w \in \Gamma_w$  and given  $u_\delta = \|\vec{v}_t\|$  from the global RANS solution in (7), seek the wall-parallel component of velocity  $u^{\text{bl}}(y)$  such that

$$\frac{\partial}{\partial y} \left( (\nu + \nu_t^{\text{bl}}) \frac{\partial u^{\text{bl}}}{\partial y} \right) = f \quad \text{in} \quad \{ \vec{x}_w - y\vec{n} \mid y \in (0, y_\delta) \} \quad (10)$$

$$u^{\text{bl}}(0) = 0, \quad u^{\text{bl}}(y_\delta) = u_\delta \quad (11)$$

where  $f = 0$  or  $f = 1/\rho dp/dx$  is assumed to be independent of  $y$  and given from the global RANS solution at  $\Gamma_\delta$ . Therein,  $\nu_t^{bl}$  is the near-wall turbulence model to be studied later. Moreover, denote  $y_\delta = \text{dist}(\vec{x}_w, \Gamma_\delta)$ . The variant  $f = 0$  is called equilibrium stress balance model leading to universal near-wall solutions.

It is well-known that for equilibrium boundary layers, e.g., the flow over a flat plate at zero pressure gradient, in the region between the wall and the outer edge of the logarithmic layer, the profiles for mean flow  $u$  and turbulence quantities  $k$ ,  $\omega$ ,  $\tilde{\nu}$  and hence  $\nu_t$  are universal, i.e., they collapse when scaled with friction velocity  $u_\tau$  and viscosity  $\nu = \mu/\rho$

$$u^+ = \frac{u}{u_\tau}, \quad y^+ = \frac{yu_\tau}{\nu}, \quad \nu_t^+ = \frac{\nu_t}{\nu}, \quad p^+ = \frac{\nu}{\rho u_\tau^3} \frac{dp}{dx}, \quad k^+ = \frac{k}{u_\tau^2}, \quad \omega^+ = \frac{\omega\nu}{u_\tau^2}$$

These universal near-wall profiles may be obtained by integration of (10) with  $f = 0$  and the corresponding 1D boundary-layer equations for  $k$  and  $\omega$  resp.  $\tilde{\nu}$ . The universal profiles for  $\nu_t^+$  are turbulence model specific in detail, but close to the mixing-length relation  $\nu_t^+ = \kappa y^+$  with near-wall damping.

It can be seen from Equation (10) in plus-units that it is the pressure gradient parameter  $p^+$  which controls the validity of the equilibrium stress balance assumption

$$(1 + \nu_t^{bl,+}) \frac{d\nu_t^{bl,+}}{dy^+} = 1 + p^+ y^+ \quad \text{in } (0, y_\delta^+). \quad (12)$$

### 3.3 Model-consistency of universal wall functions and grid-independent predictions

Universal wall functions are the solution of (10) with  $f = 0$  written in non-dimensional form

$$(1 + \nu_t^{bl,+}) \frac{d\nu_t^{bl,+}}{dy^+} = 1 \quad \text{in } (0, y_\delta^+) \quad (13)$$

A universal wall-function method is called *consistent* w.r.t. the turbulence model used, if the low-Re RANS solution for a flat-plate zero-pressure gradient boundary layer flow also solves (13). This implies  $\nu_t^{bl} = \nu_t$ , i.e., wall functions have to be turbulence-model specific, as revealed by [1]. Consistency ensures that  $u = u^{bl}$  in the entire near-wall region  $\Omega_\delta$ , cf. [14, 2]. Then predictions for surface transfer coefficients like  $c_p$ ,  $c_f$  are independent of the location of the matching boundary  $\Gamma_\delta$  which consists of the first grid nodes above the wall. Thus turbulence-model consistent universal wall functions give (almost) grid-independent predictions at least for flows close to equilibrium.

Except the novel approach [1], existing wall-function methods are not model-consistent, as they use the algebraic model for  $\nu_t^{bl}$  by Spalding [13], see e.g. [4], or an approximative hybrid law of the wall for  $u^{bl}$ , see e.g. [5]. The deviation from the turbulence model specific RANS solution in the buffer layer is discernible in Figure 2 (left) and causes grid-dependent results.

As the near-wall profiles of different versions of the Spalart-Allmaras model resp. the  $k-\omega$  model almost collapse, see [2], [3], it is sufficient to determine one model-consistent universal

wall-function for the Spalart-Allmaras model and one for the  $k$ - $\omega$  model

$$F_{SA,a} = (1 - \phi_{SA})F_{Sp,5} + \phi_{SA}F_{Rei,m}, \quad \phi_{SA} = \tanh(\arg^3), \quad \arg = y^+/24 \quad (14)$$

$$F_{k\omega,a} = (1 - \phi_{k\omega})F_{Sp,3} + \phi_{k\omega}F_{Rei,m}, \quad \phi_{k\omega} = \tanh(\arg^2), \quad \arg = y^+/50 \quad (15)$$

which are plotted in Figure 2 (right). Therein, we use Reichardt's law of the wall

$$u^+ = F_{Rei}(y^+), \quad F_{Rei}(y^+) \equiv \frac{\ln(1 + 0.4y^+)}{\kappa} + 7.8 \left( 1 - e^{-\frac{y^+}{11.0}} - \frac{y^+}{11.0} e^{-\frac{y^+}{3.0}} \right). \quad (16)$$

and use the fact that Reichardt's law blended with the classical log-law  $F_{log} = \ln(y^+)/\kappa + 5.1$  gives an excellent agreement in the log-layer when using the formula

$$F_{Rei,m} = (1 - \phi_{b1})F_{Rei} + \phi_{b1}F_{log}, \quad \phi_{b1} = \tanh(\arg^4), \quad \arg = y^+/27. \quad (17)$$

Spaldings law [13] with parameter  $N \in \{3, 4, 5\}$  is given by the inverse formula

$$y^+ = F_{Sp,N}^{-1}(u^+), \quad F_{Sp,N}^{-1}(u^+) \equiv u^+ + e^{-\kappa \cdot 5.2} \left( e^{\kappa u^+} - \sum_{n=0}^N \frac{(\kappa u^+)^n}{n!} \right). \quad (18)$$

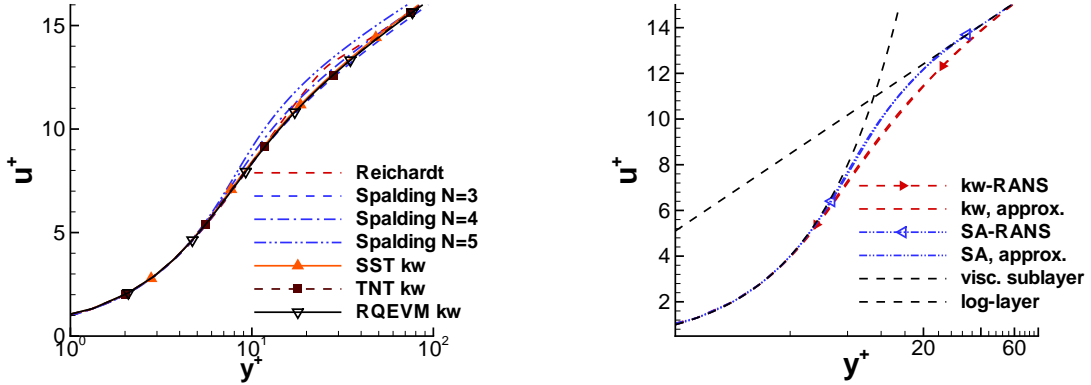


Figure 2: Classical inconsistent wall-functions (17), (18) and near-wall profiles for different  $k$ - $\omega$  type models (left) and model-consistent universal wall-functions for SA- and  $k$ - $\omega$  model (right).

### 3.4 Flat plate turbulent boundary layer at zero pressure gradient

The ability of the new wall function proposal to give solutions independent of the wall-normal grid is studied for the boundary layer flow at zero pressure gradient by Wieghardt and Tillmann, recorded in [15], pp. 98-123, as Flow 1400. In agreement with the experimental setup we use  $u_\infty = 33\text{ms}^{-1}$ ,  $\nu = 1.51 \times 10^{-5}\text{m}^2\text{s}^{-1}$  and the length of the plate is  $l = 5\text{m}$ . Hybrid but

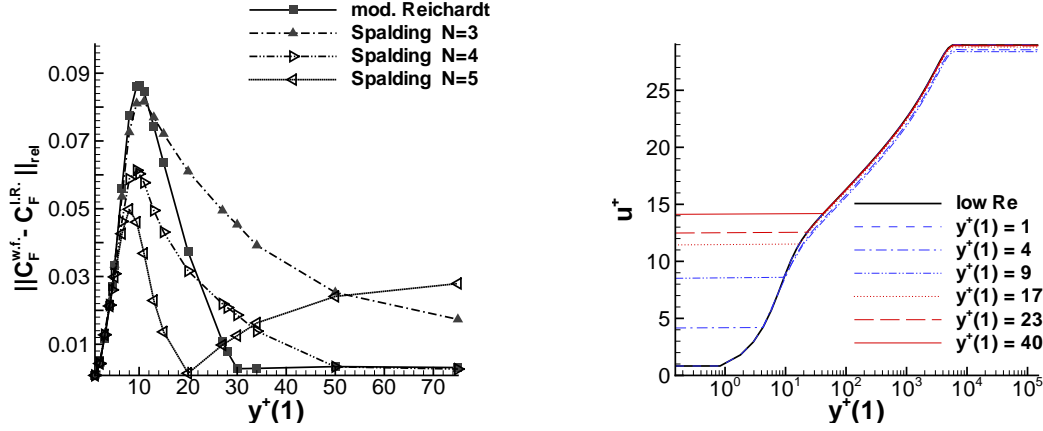


Figure 3: Review of classical hybrid wall laws (17), (18) for SA-Edwards model (left) and velocity profiles for new analytical wall law (14) on grids with different  $y^+(1)$  for SA-E model (right).

inconsistent wall functions (17), (18) show a relatively large deviation from the low-Re solution if  $y^+(1) \approx 12$ , see Figure (3) (left).

The model-consistent formulas (14) and (15) give almost grid independent predictions for  $c_f$  for the SA-Edwards model and the Baseline  $k-\omega$  model resp., see Figure 4. Moreover the near-wall velocity profiles almost collapse, see Figure 3 (right) and Figure 5 (right). We mention that the remaining slight grid-dependence is due to numerical errors, see [1] for details.

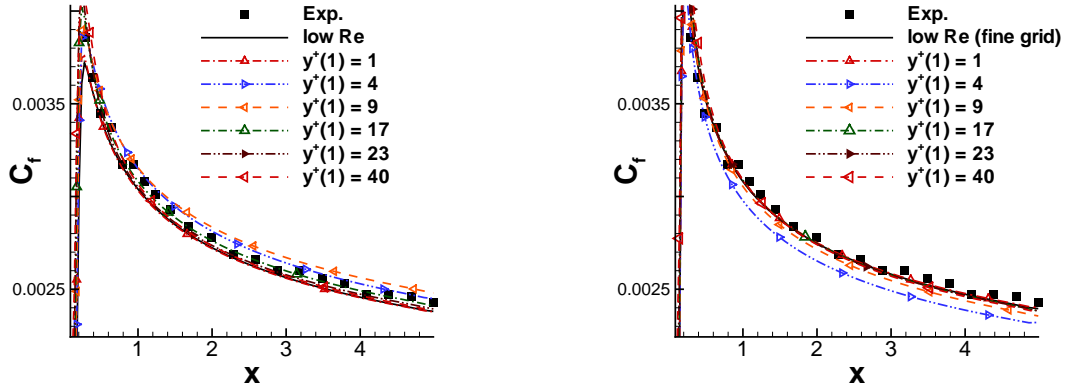


Figure 4: Analytical model-consistent wall-function Eq. (14) for SA-E model (left) and Eq. (15) for Baseline  $k-\omega$  model (right).

In order to obtain grid independent results for  $k-\omega$  type models, it is crucial to replace the standard (sqrt) blending [6] by a new proposal. As shown in Figure 5 (left), the standard blending (19) deviates discernibly from the low-Re RANS solution for  $\omega$  in the buffer layer. This causes

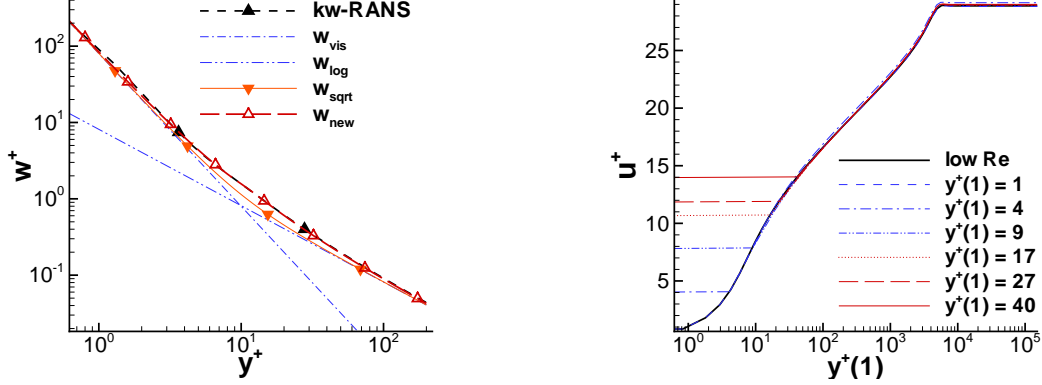


Figure 5: Left: Near-wall RANS solution and wall-functions (19), (20) for  $\omega$ . Right: Velocity profiles for the analytical wall-function (15) on grids with different  $y^+(1)$  for the Baseline  $k$ - $\omega$  model.

grid-dependent results, as demonstrated in Figure 6 (right).

$$\text{Standard (sqrt) blending: } \omega = \sqrt{\omega_{\text{vis}}^2 + \omega_{\text{log}}^2}, \quad (19)$$

$$\text{New proposal: } \omega = \phi \omega_{\text{b1}} + (1 - \phi) \omega_{\text{b2}}, \quad \phi = \tanh(\arg^4), \quad \arg = \frac{y^+}{10} \quad (20)$$

with the blending formula and the asymptotic relations

$$\omega_{\text{b1}} = \omega_{\text{vis}} + \omega_{\text{log}}, \quad \omega_{\text{b2}} = (\omega_{\text{vis}}^{1.2} + \omega_{\text{log}}^{1.2})^{1/1.2} \quad (21)$$

$$\omega_{\text{vis}} = \frac{6\nu}{\beta_\omega y^2}, \quad \omega_{\text{log}} = \frac{u_\tau}{\sqrt{\beta_k \kappa y}}. \quad (22)$$

Moreover, we recommend to use Wilcox b.c. (5) instead of Menter b.c. (4) (recall that the latter was designed for low-Re grids), see Figure 6 (left). We finally mention that formula (15) gives almost grid-independent results also for other variants of the  $k$ - $\omega$  model, see Figure 7 for the  $k$ - $\omega$ -EARSM [21] and the  $k$ - $\omega$  RQEVm [20].

#### 4 A PRIORI INVESTIGATION FOR APPLICATION OF WALL-FUNCTIONS TO AERODYNAMIC FLOWS

Aerodynamic flows around airfoils, blades etc. are characterised by the presence of (i) stagnation points and subsequent not yet fully developed turbulent flow, (ii) regions of adverse pressure gradient with relatively large pressure gradient parameter, and (iii) regions of separation and reattachment. In order to apply universal wall-functions for flow situations (i)-(iii), we have to ensure that the near-wall RANS solutions are close to the universal wall functions in  $\Omega_\delta$ . In flow situations (i) and (iii), the universal wall functions are a good approximation if  $y^+(1) \lesssim 10$ , see [1] for (iii) and [3] for (i). In this paper we only consider situation (ii), which is strongly relevant for highlift configurations, for more details see [3].

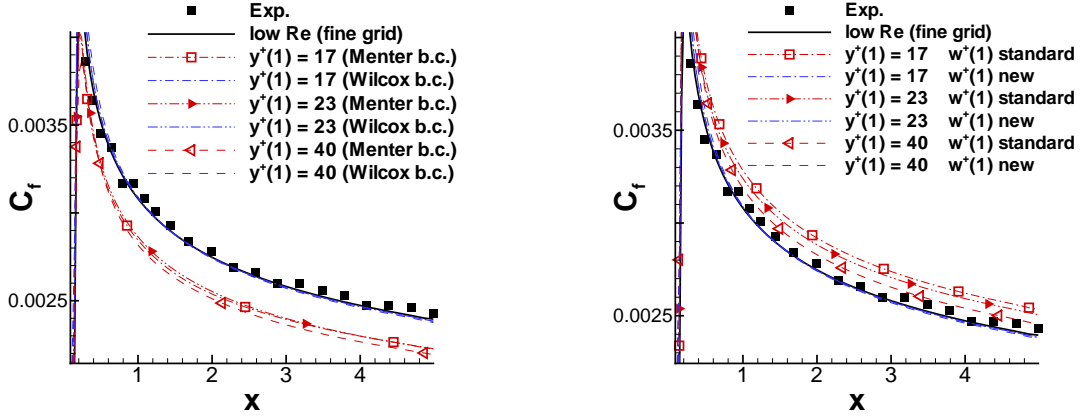


Figure 6: Left: Comparison of different boundary conditions by Menter (4) and by Wilcox (5). Right: Standard wall-function formula for  $\omega$  (19) and new proposal (20) for Baseline  $k-\omega$  model.

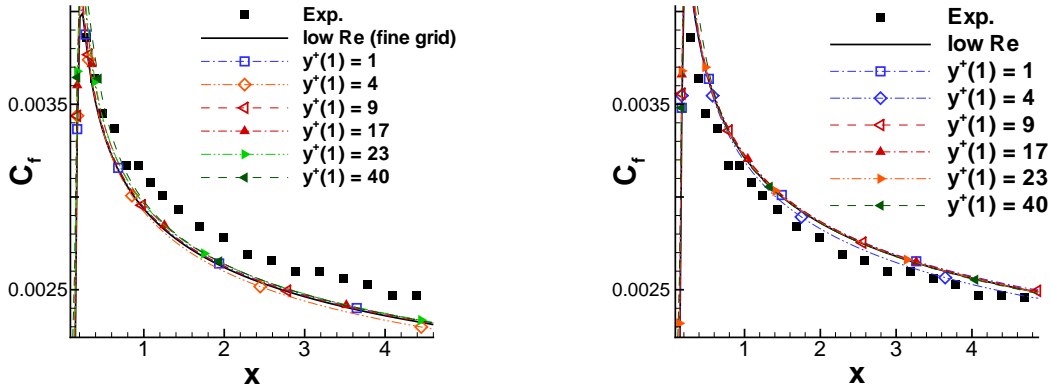


Figure 7: Predictions for  $C_f$  for EARSM  $k-\omega$  [21] (left) and RQEVm  $k-\omega$  [20] (right).

#### 4.1 Near-wall behaviour of RANS turbulence models in adverse pressure gradient flows with separation

As indicated by Equation (12), in attached fully developed turbulent boundary layer flow, the range of validity of zero-pressure gradient wall-functions is determined by the size of  $p^+$ . Note that  $p^+$  is positive for adverse pressure gradients and negative for favourable pressure gradients. Due to its definition,  $p^+$  goes to infinity as the stagnation and separation points are approached. Moreover, the size of  $p^+$  becomes larger as Reynolds number is decreased. Figure 8 shows the Reynolds number dependence of the  $p^+$ -distribution on the upper side of the A-airfoil at  $\alpha = 13.3^\circ$ . With regard to the application of wall-functions, the fact that  $u_\tau \rightarrow 0$  as separation is approached has two counteracting effects.

The *unfavourable* effect is that for constant  $dp/dx$  close before separation  $p^+ \rightarrow \infty$  such that the universal ZPG profiles for  $u$  (and  $\omega$ ) cease to be valid. For this purpose we study the flow

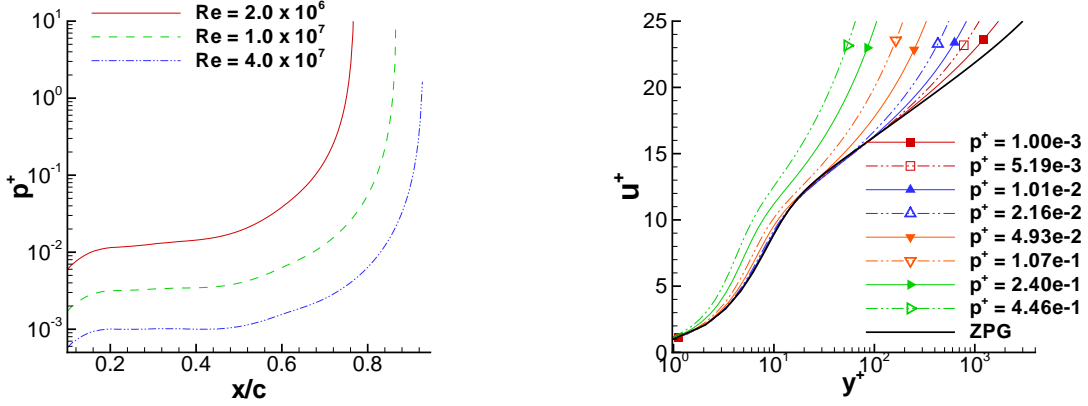


Figure 8: Reynolds number dependence of  $p^+$  (left) and  $p^+$ -dependent near-wall behaviour (right) for SA-E model.

over a flat plate at  $Re = 4.1 \times 10^7$  devised by [1]. We use a flat plate of length  $L = 8\text{m}$  with farfield data  $u_\infty = 78\text{ms}^{-1}$  and  $\nu_\infty = 1.5 \times 10^{-5}\text{m}^2\text{s}^{-1}$ . At distance  $y = 0.5\text{m}$  above the wall, suction and blowing is imposed by prescribing the wall-normal velocity component  $v(x) = A \exp(-b(x - x_\alpha)^2) - A \exp(-b(x - x_\beta)^2)$  with  $x_\alpha = 2.5$ ,  $x_\beta = 5.5$ ,  $A = 0.35x$ ,  $b = 108/6^2$  which produces a streamwise pressure gradient leading to separation.

The SST  $k-\omega$  model shows a general breakdown of the universal ZPG solution, i.e., the character of the velocity profile changes over the entire intermediate region ( $5 < y^+ < 50$ ) and log-layer ( $y^+ > 50$ ), see Figure 9. This is due to the large deviation for  $k$  from its universal ZPG solution, see Figure 10 (left). However, in the viscous sublayer ( $y^+ < 5$ ) agreement with the universal ZPG solution is still very close, except at large  $p^+$ -values very close before separation. On the other hand, the SA-E model shows a successive breakdown of the universal ZPG solution, i.e., the region occupied by the universal ZPG solution is reduced progressively, see Figure 8 (right).

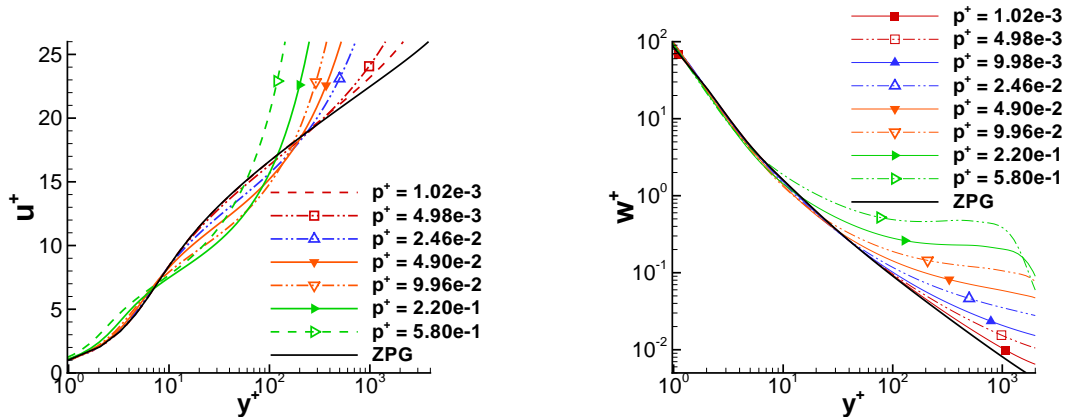


Figure 9: Near-wall solutions for SST  $k-\omega$  model at different  $p^+$ -stations for APG flow [1].

The *favourable* point is that the thickness of the viscous sublayer in dimensional units is becoming larger, i.e., points at a given constant wall-distance located in the log-layer upstream of the separation point now may reside in the viscous sublayer. This effect is illustrated in Figure 10 (right). Therein, we consider wall-parallel grid-lines and study their  $y^+$  distribution on the upper side of the A-airfoil at  $\alpha = 13.3^\circ$ . As the separation point is approached, their  $y^+$ -values move toward the viscous sublayer.

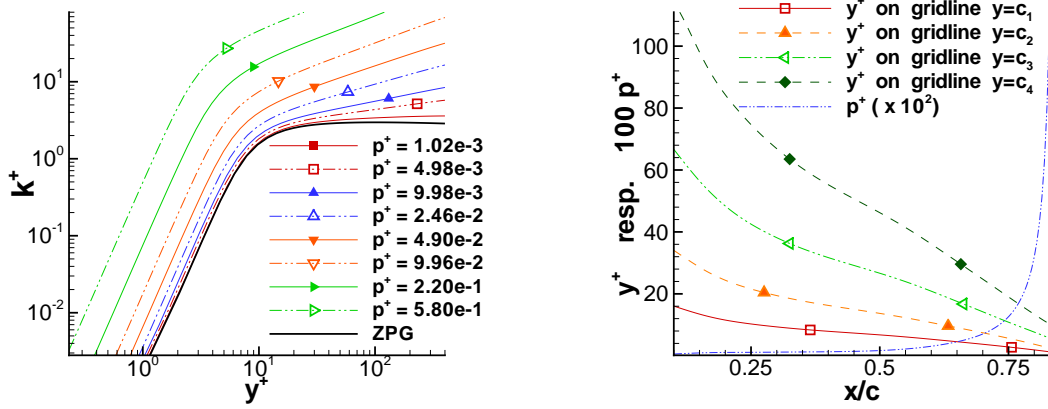


Figure 10: Left: Near-wall profiles of  $k$  for APG flow [1]. Right: Wall-distance in plus-units for wall-parallel grid-lines in APG flow around A-airfoil.

## 4.2 Implications for design of universal wall-function methods for aerodynamic flows

Thus in adverse pressure gradient flows, the universal wall-functions (14), (15) are still a close approximation to the low-Re RANS solution, provided the first off-wall node is located at a  $y^+$ -location where the departure from the universal solution is not yet large with respect to the corresponding  $p^+$ -value. This can be ensured by a near-wall grid adaptation with a sensor based on the local  $p^+$ -value, see [3].

At the leading edge, in the region of stagnation point and not yet fully developed turbulent flow, for  $y^+(1) \lesssim 10$  the universal wall-functions are also a close approximation. For larger  $y^+(1)$  the deviation becomes more pronounced, in particular for the SA model, see [3]. The viscous sublayer at the leading edge is relatively thin as the strongly accelerated flow around the suction peak has a relatively large  $c_f$ . Ensuring that  $y^+(1)$  is located in the viscous sublayer requires a near-wall adaptation even on intermediate-Re grids. In the region of separation and reattachment, the universal ZPG profile is a good approximation for local values of  $y^+(1) \lesssim 10$ , see [1]. Due to the relatively small  $c_f$ , the viscous sublayer is relatively thick in the separation region and no adaptation may be required on intermediate-Re grids.

We remark that off-wall boundary conditions for  $k$  and  $\tilde{\nu}$  using the universal ZPG solution for  $k$  and  $\tilde{\nu}$  are sources of grid-dependent results, see also [3]. Instead, we prescribe  $k = 0$  and  $\tilde{\nu} = 0$  on  $\Gamma_w$ .

## 5 NUMERICAL METHOD

The numerical results are obtained using the DLR TAU-code, the unstructured finite-volume solver developed at DLR, which is of cell-vertex type, i.e., of cell-centered type w.r.t. the dual grid cells. The convective fluxes are calculated by a central scheme with artificial scalar dissipation [16]. The gradients of the flow variables are reconstructed using a Green-Gauss-MUSCL formula. The arising fixed-point problem is iterated in fictitious pseudo-time using a low-storage k-stage Runge-Kutta scheme by Jameson [17].

The wall-shear stress prescribed in (6) is given by  $\tau_w^{bl} = \rho u_\tau^2$ , where  $u_\tau$  is computed as follows. Suppose a solution of (10) with  $f = 0$  is known in either of the two closed forms

$$u^+ = F(y^+) \Leftrightarrow \frac{u}{u_\tau} = F\left(\frac{y u_\tau}{\nu}\right) \quad \text{or} \quad y^+ = F^{-1}(u^+) \Leftrightarrow \frac{y u_\tau}{\nu} = F^{-1}\left(\frac{u}{u_\tau}\right) \quad (23)$$

then the matching condition  $u^{bl} = u_\delta$  on  $\Gamma_\delta$  and the relation  $u^{bl} = u_\tau F(y u_\tau / \nu)$  imply

$$F\left(\frac{y_\delta u_\tau}{\nu}\right) = \frac{u_\delta}{u_\tau} \quad \text{resp.} \quad F^{-1}\left(\frac{u_\delta}{u_\tau}\right) = \frac{y_\delta u_\tau}{\nu} \quad (24)$$

which can be solved for  $u_\tau$  using Newton's method. Denote  $\text{TM} \in \{\text{SA}, k\omega\}$  and  $N \in \{3, 5\}$ . For the numerical solution of

$$\frac{u_\delta}{u_\tau} = F_{\text{TM}}\left(\frac{y_\delta u_\tau}{\nu}\right), \quad F_{\text{TM}} = (1 - \phi_{\text{TM}})F_{\text{S,N}} + \phi_{\text{TM}}F_{\text{Rei,m}}$$

we proceed as follows:

1. From the initial guess  $u_\tau^0 = u_\delta / y_\delta$ , seek  $u_{\tau, \text{Rei}}$  as solution of  $u_\delta / u_\tau = F_{\text{Rei,m}}(y_\delta u_\tau / \nu)$ .
2. Using the initial guess  $u_\tau^0 = u_{\tau, \text{Rei}}$ , seek  $u_{\tau, \text{S}}$  as solution of  $y_\delta u_\tau / \nu = F_{\text{S,N}}^{-1}(u_\delta / u_\tau)$ .
3. Compute  $\phi_{\text{TM}}$  and set  $u_\tau = (1 - \phi_{\text{TM}})u_{\tau, \text{S}} + \phi_{\text{TM}}u_{\tau, \text{Rei}}$ .

Convergence in steps (1) and (2) is achieved after three to four iteration steps.

## 6 APPLICATION TO AERODYNAMIC FLOWS WITH SEPARATION

### 6.1 Transonic airfoil flows RAE-2822 cases 9 and 10

We apply the method to the transonic airfoil flows RAE-2822 case 9 (no/small separation region at  $Ma = 0.73$ ,  $Re = 6.5 \times 10^6$  and angle of attack  $\alpha = 2.8^\circ$ ) and case 10 (shock induced separation at  $Ma = 0.75$ ,  $Re = 6.2 \times 10^6$  and  $\alpha = 2.8^\circ$ ) studied experimentally in [18]. We use a series of hybrid-Re grids of O-type with  $y^+(1)$  varying from one to 60, generated using the commercial grid generation tool CentaurSoft ([www.centaursoft.com](http://www.centaursoft.com)). The corresponding  $y^+(1)$ -distribution for the SST  $k-\omega$  model is given in Figure 11. The grids are built such that the thickness of the prismatic layer has an almost constant value around  $0.052c$  (with chord length  $c$ ) and fully contains the boundary layer.

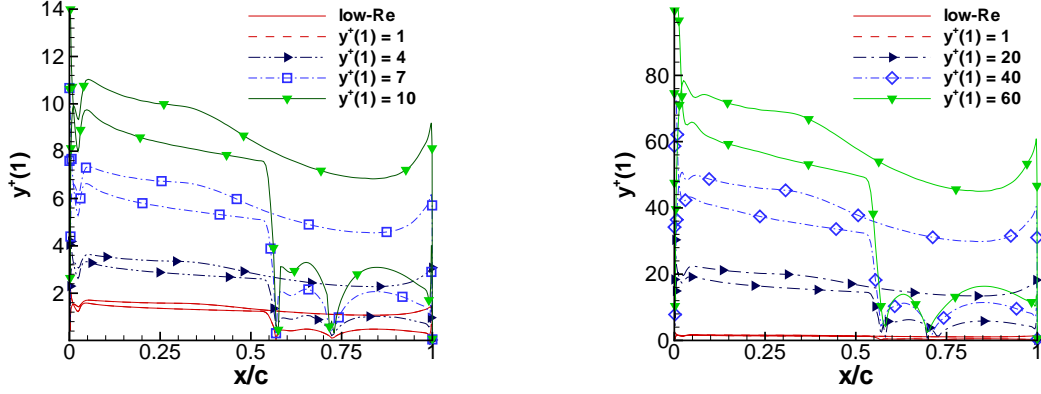


Figure 11: RAE case 10: Distribution of  $y^+(1)$  for SST  $k-\omega$  model.

The predictions for the pressure coefficient  $c_p$  and the local skin friction coefficient  $c_f^{(loc)}$  (based on the local dynamic pressure at the boundary layer edge  $q_P$ , [18]) are given in Figures 12-15. For the SA-E model, the prediction of  $c_p$  is remarkably grid-independent, in particular regarding the shock position. The predictions of  $c_f$  for  $y^+(1) = 1$  and  $y^+(1) \gtrsim 20$  almost collapse whereas

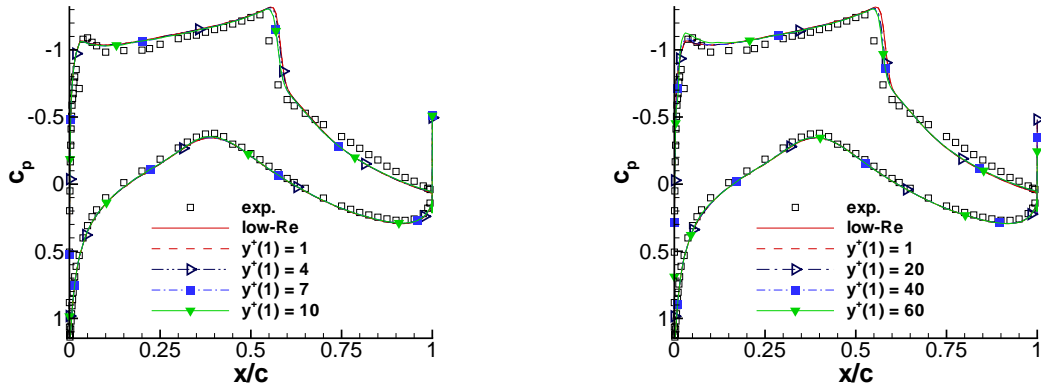
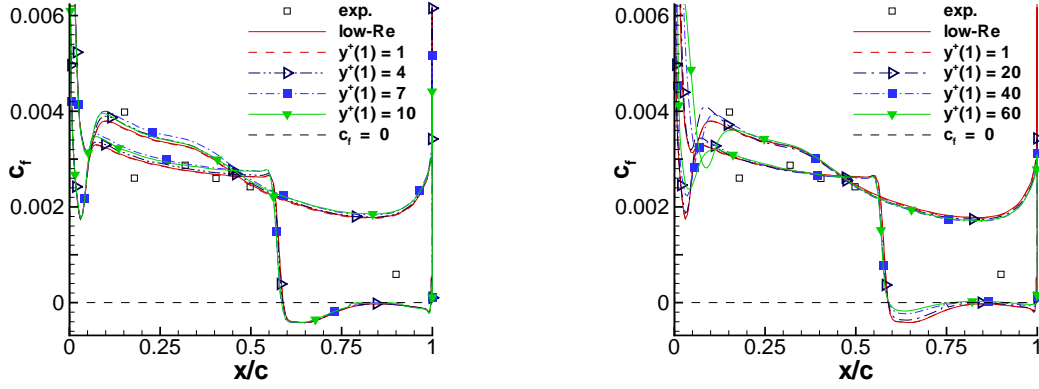
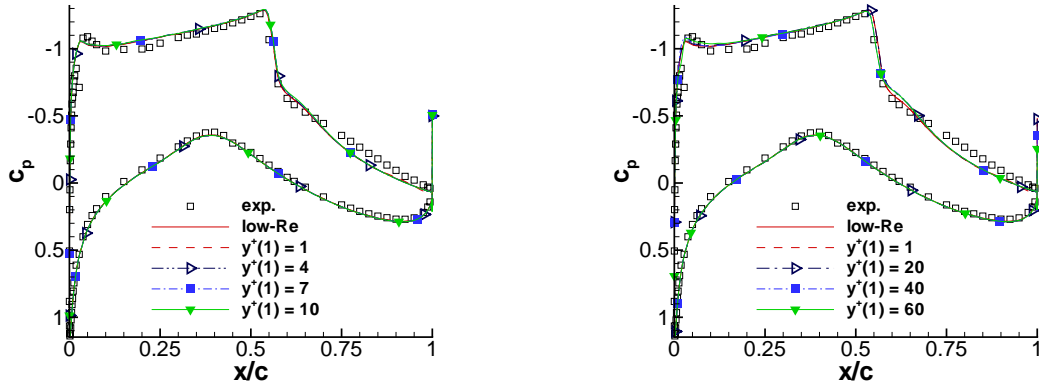


Figure 12: RAE case 10: Distribution of  $c_p$  for the SA-E model.

in the region of intermediate values of  $y^+(1)$  the deviation is slightly larger. In the separation region, the agreement on intermediate-Re grids with  $y^+(1) \lesssim 10$  is surprisingly close, whereas on the coarser grids  $y^+(1) \gtrsim 20$  the differences become more pronounced.

Concerning the SST  $k-\omega$  model, the prediction of  $c_p$  is again almost grid-independent. In the fully turbulent region on the upper side before the shock, there are moderate deviations in  $c_f$  on the intermediate-Re and high-Re grids.

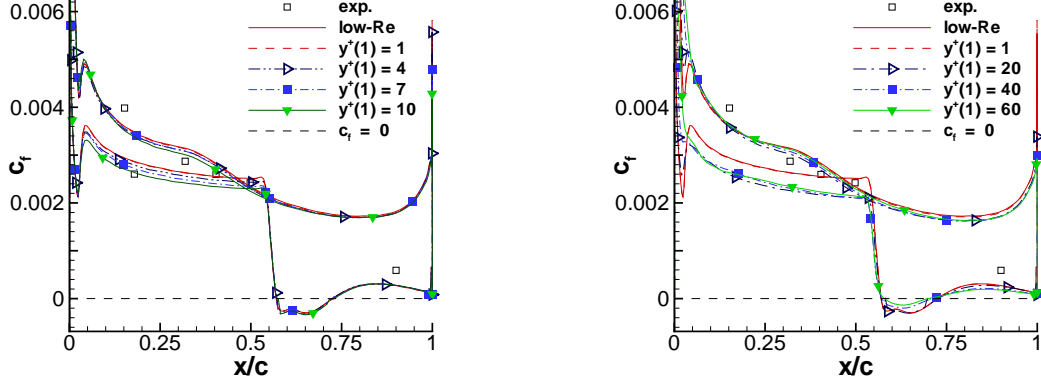
Finally, the grid-dependent spreading is assessed by reference with other sources of uncertainty. The grid-dependence using wall-functions is 1% in  $C_l$  on all grids, and 4% in  $C_d$  if  $y^+(1) \lesssim 10$ .

Figure 13: RAE case 10: Distribution of  $c_f$  for the SA-E model.Figure 14: RAE case 10: Distribution of  $c_p$  for SST  $k-\omega$  model with Wilcox b.c.

However, the difference between SA-E and SST  $k-\omega$  model is 3% in  $C_l$  and 3% in  $C_d$ , the difference between various  $k-\omega$  model versions (TNT model [19], LEA model [20], and SST model) is 4% in  $C_l$ , and 5%  $C_d$ . Moreover, different grid topologies (O-type vs. H-type) cause a spreading of 1% in  $C_l$  and 2%  $C_d$ . Different implementations of the momentum boundary condition (no-slip vs. low-Re wall-shear stress) lead to a spreading of 2% in  $C_l$  and 4% in  $C_d$ .

## 6.2 Subsonic A-airfoil in highlift configuration

In this section the wall-function method is applied to the subsonic flow around the "A-airfoil" in highlift configuration at  $Ma = 0.15$ ,  $Re = 2.0 \times 10^6$ , and  $\alpha = 13.3^\circ$ , studied experimentally in [22, 23]. On the upper side of the airfoil, the strong adverse pressure gradient causes the turbulent boundary layer to separate close to the trailing edge. In the experiment, transition was prescribed at  $x/c = 0.3$  on the lower side and free transition was observed at  $x/c = 0.12$  on the upper side, but in the present computations the airfoil surface is treated fully turbulent.

Figure 15: RAE case 10: Prediction of  $c_f$  for SST  $k$ - $\omega$  model with Wilcox b.c.

$y^+(1)$	$N_y$	$C_l$	$C_d$
low-Re	37	0.7677	0.0258
1	37	0.7672	0.0257
4	34	0.7717	0.0258
7	31	0.7740	0.0255
10	29	0.7751	0.0248
20	26	0.7761	0.0230
40	22	0.7702	0.0217
60	20	0.7720	0.0215

Turb. model	$C_l$	$C_d$
Exp.	0.743	0.0242
SA-E	0.761	0.0254
LEA $k$ - $\omega$	0.760	0.0260
SST low-Re	0.737	0.0247
SST hyb-Re	0.725	0.0238
TNT low-Re	0.769	0.260
TNT hyb-Re	0.756	0.251

Table 1: Aerodynamic coefficients for RAE2822. Left: Predictions using wall functions. Right: Spreading depending on different turbulence models and on the choice of momentum boundary condition on an H-type grid.

It is noteworthy that neglecting transition increases the deviation from the experimental data significantly.

The  $y^+(1)$ -distributions for the series of O-type grids are shown in Fig. 16, where the nominal value has to be seen as an average over the chord length. Regarding the SA-E model, the predictions on the grids with  $y^+(1) \leq 10$  are shown in Figure 17 and are in close agreement with the low-Re solution. The two solutions with  $y^+(1) = 40$  and  $y^+(1) = 80$  suffer from local oscillations in  $c_p$  near the leading edge and are not shown here. This can be remedied by ensuring smaller values for  $y^+(1)$  near the leading edge by using a near-wall grid adaptation. For the SST  $k$ - $\omega$  model with the Wilcox b.c. (see Figure 18), on all grids the agreement in  $c_f$  with the low-Re solution is remarkably good, in particular for  $y^+(1) \lesssim 10$ . It is worthwhile mentioning that for the SST model, the spreading in the separation point is 1% for  $y^+(1) \lesssim 24$  and even only 4% on the coarsest mesh with  $y^+(1) \approx 80$ . In contrast, the predictions of the separation point between SST and SA-E model differ by 11%.

As a final remark, the grid-dependent spreading using wall-functions can be reduced further by

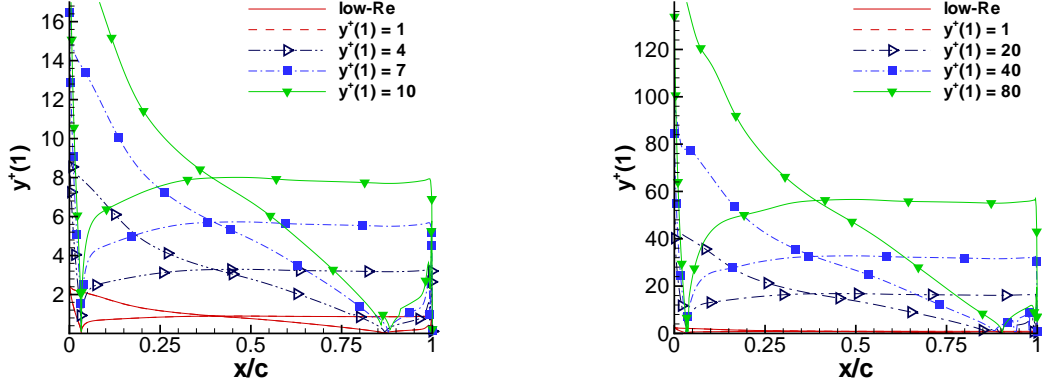


Figure 16: A-airfoil: Distribution of  $y^+(1)$  for the SST  $k-\omega$  model.

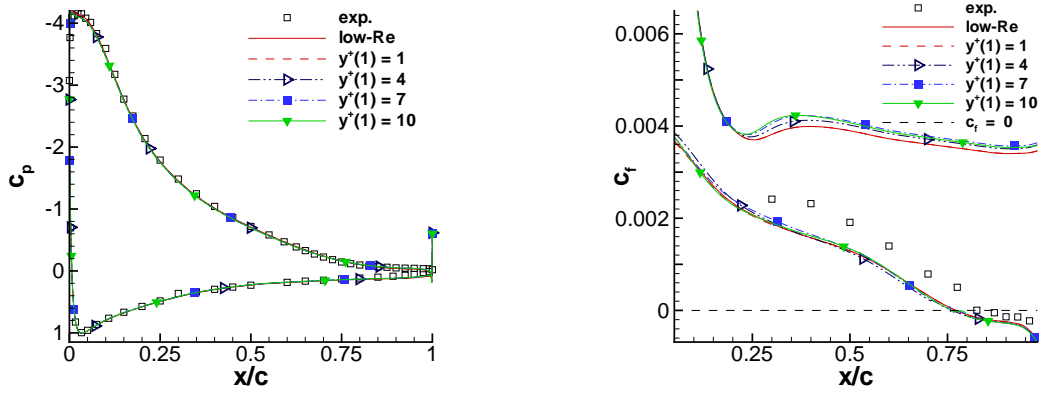


Figure 17: A-airfoil: Prediction for  $c_p$  (left) and  $c_f$  (right) for SA-E model.

applying a near-wall grid adaptation technique with respect to  $y^+(1)$  to ensure that  $y^+(1) \in [5, 10]$  near the leading edge, and  $y^+(1) \in [1, 5]$  close to the separation point and in regions of separated flow, see [3] for details.

## 7 DISCUSSION OF OTHER WALL-FUNCTION APPROACHES

Finally, as suggested by the conference committee, we discuss the approach by Grotjans and Menter [7], [8], which introduces the concept of a virtual wall, see Figure 18 (right). Consider a grid for the original domain  $\Omega$  with wall nodes on the physical no-slip wall  $\Gamma_w$  (hence at wall-distance  $y(0) = 0$ ) and first off-wall nodes on  $\Gamma_\delta$  at distance  $y(1) = y_\delta$  from  $\Gamma_w$ . The idea is now to replace  $\Omega$  by  $\tilde{\Omega} = \Omega \cup \tilde{\Omega}_{\text{vis,virt}}$  where

$$\tilde{\Omega}_{\text{vis,virt}} = \{ \vec{x}_w + y\vec{n}, \vec{x}_w \in \Gamma_w, 0 \leq y < \tilde{y}(0) \}$$

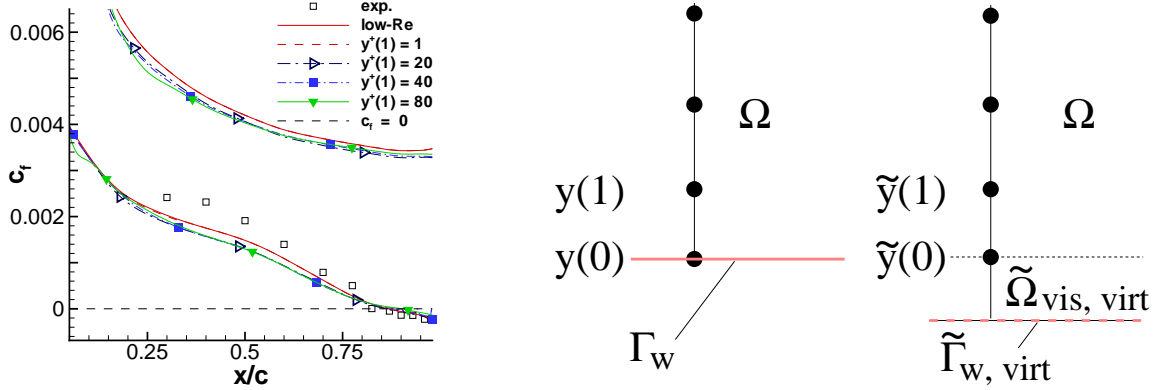


Figure 18: Left: Prediction for  $c_f$  for SST  $k$ - $\omega$  model with Wilcox b.c. for A-airfoil. Right: Virtual wall approach by Grotjans and Menter [7].

where  $\vec{n}$  is the outer normal vector to  $\Gamma_w$ ,  $\Gamma_w$  denotes the no-slip wall of the original domain  $\Omega$ , and  $\tilde{y}(0)$  has to be specified later. The set of points  $\tilde{\Gamma}_{w, virt} = \{ \vec{x}_w + \tilde{y}(0)\vec{n} \mid \vec{x}_w \in \Gamma_w \}$  can be interpreted as the virtual wall of the domain  $\tilde{\Omega}$ .

Then in (1)-(9),  $\Omega$ ,  $\Gamma_w$  are replaced by  $\tilde{\Omega}$ ,  $\tilde{\Gamma}_{w, virt}$ , but the same computational grid is used for  $\tilde{\Omega}$  as for  $\Omega$ . Then the grid nodes  $y(0)$  on  $\Gamma_w$  are the first off-wall nodes w.r.t.  $\tilde{\Gamma}_{w, virt}$  with wall-distance  $\tilde{y}(0)$ .

On  $\tilde{\Omega}$ , denote  $\tilde{u}(0)$  the wall-parallel velocity at  $\tilde{y}(0)$ . Then [7], [8] seek  $u_\tau$  and  $\tilde{y}(0)$  such that

$$\frac{\tilde{u}(0)}{u_\tau} = F_{\log} \left( \frac{\tilde{y}(0)u_\tau}{\nu} \right) = \frac{1}{\kappa} \ln \left( \frac{\tilde{y}(0)u_\tau}{\nu} \right) + 5.1 \quad (25)$$

$$\frac{\tilde{y}(0)u_\tau}{\nu} = 11.06 \quad (26)$$

which can be solved explicitly for  $u_\tau$  and then  $\tilde{y}(0)$  can be obtained. Thus the location of the virtual wall is determined such that  $\tilde{y}(0)$  is located at the intersect of asymptotic profiles for viscous sublayer and log-layer, see Figure 2 (right), which is approximately the outer edge of the viscous sublayer.

In (25)-(26), the wall distance of the first node above the physical wall  $y(1)$  does not appear. However, this method assumes that the log-law is a good approximation for the near-wall behaviour of the  $k$ - $\omega$  turbulence model in  $11.06 \leq y^+ \lesssim 50$ , which is obviously not the case, see Figure 2 (right). This turbulence-model inconsistency can be seen from the poor reproduction of the log-law on different grids for a flat plate turbulent boundary layer at ZPG, see [8], p.77.

A similar method has been proposed by Vieser and Menter [6], which is inspired by [7], [8]. Therein  $u_\tau$  is computed from

$$\frac{u_\delta}{u_\tau} = F_{\log} \left( \frac{\tilde{y}_\delta u_\tau}{\nu} \right), \quad \frac{\tilde{y}_\delta u_\tau}{\nu} = \max \left( \frac{y_\delta u_\tau}{\nu}, 11.06 \right) \quad (27)$$

Again, (27) uses the log-law, or equivalently  $\nu_t^{bl,+} = \kappa y^+ - 1$ , which is obviously not-consistent neither with the  $k-\omega$  model nor with the SA model. Thus both approaches cannot be expected to give grid-independent predictions even for flat plate boundary layer flows at ZPG.

Now the approaches [6], [7], [8] are studied for non-equilibrium flows. Recall the typical  $y^+$ -distribution in a flow with separation induced by a smooth adverse pressure gradient in Figure 10 (right). Then the virtual-wall switch  $y^+ \leq 11.06$  is "activated" inevitably close before separation. For  $y^+ < 11.06$ , both methods compute  $u_\tau$  from the low-law, which deviates largely from the low-Re RANS solution, in particular at large  $p^+$ -values. However, [8] does not present such a test case with separation caused by a smooth APG. Regarding the prediction of separation region and reattachment, the grid-independence of the results using turbulence model specific wall-functions in [1] pp.282, is clearly superior to the results in [7] p.1117.

## 8 CONCLUSIONS

A turbulence-model specific wall function method has been presented which gives (almost) grid-independent results for aerodynamic flows with separation in the subsonic and transonic regime. The treatment of laminar-turbulent transition and effects of strong compressibility in hypersonic flows will be subject of future research.

## REFERENCES

- [1] G. Kalitzin, G. Medic, G. Iaccarino and P. Durbin. Near-wall behaviour of RANS turbulence models and implications for wall functions. *J. Comput. Phys.*, **204**, 265–291, (2005).
- [2] T. Knopp. A new adaptive wall-function method for subsonic and transonic turbulent flows. *DLR IB 224-2005 A 14*, (2005).
- [3] T. Knopp, T. Alrutz and D. Schwamborn. A grid and flow adaptive wall-function method for RANS turbulence modelling. *J. Comput. Phys.* (accepted).
- [4] N.T. Frink. Tetrahedral unstructured Navier-Stokes method for turbulent flows. *AIAA J.*, **36**, 1975–1982, (1998).
- [5] B. Mohammadi and G. Medic. A critical evaluation of the classical  $k/\epsilon$  model and wall-laws for unsteady flows over bluff bodies. *INRIA, Rapport de recherche no. 3056*, (1996).
- [6] W. Vieser and T. Esch and F.R. Menter. Heat transfer predictions using advanced two-equation turbulence models. *CFX Technical Memorandum CFX-VAL10/0602*, (2002).
- [7] H. Grotjans and F. Menter. Wall functions for general application CFD codes. *ECCOMAS 1998, Vol 1, part 2*, 1112–1117 (1999).
- [8] H. Grotjans. Turbulenzmodelle höherer Ordnung für komplexe Anwendungen (in German). *PhD thesis, TU Munich, VDI Verlag*, (1999).

- [9] P.R. Spalart and S.R. Allmaras. A one-equation turbulence model for aerodynamics flows. *AIAA Paper 1992-0439*, (1992).
- [10] J.R. Edwards and S. Chandra. Comparison of eddy viscosity-transport turbulence models for three-dimensional, shock separated flowfields. *AIAA J.*, **34**, 756–763, (1996).
- [11] F.R. Menter. Zonal two equation  $k/\omega$  turbulence models for aerodynamic flows. *AIAA Paper 1993-2906*, (1993).
- [12] D.C. Wilcox. *Turbulence modeling for CFD*, DWC Industries, (1998).
- [13] D.B. Spalding. A single formula for the law of the wall. *J. Appl. Mech.*, **28**, 455-457, (1961).
- [14] M.D. Tidriri. Domain decomposition for compressible Navier-Stokes equations with different discretizations and formulations. *J. Comput. Phys.*, **119**, 271–282, (1995).
- [15] D. E. Coles and E. A. Hirst (Eds.) *Computation of Turbulent Boundary Layers - 1968 AFOSR-IFP-Stanford Conference*, Stanford, (1969).
- [16] D.J. Mavriplis and A. Jameson and L. Martinelli. Multigrid solution of the Navier-Stokes equations on triangular Meshes. *ICASE-report No. 89-35*, (1989).
- [17] A. Jameson. Transonic Flow Calculations. *MAE Report 1651, Princeton University*, (1983).
- [18] P. H. Cook, M. A. McDonald and M.C.P. Firmin. Aerofoil RAE 2822 - Pressure distributions and boundary layer and wake measurements. *AGARD Advisory Report AR-138, A6.1-A6.77*, (1979).
- [19] J.C. Kok. Resolving the dependence on freestream values for the  $k/\omega$  turbulence model. *AIAA J.*, **38**, 1292–1295, (2000).
- [20] T. Rung, H. Lübcke, M. Franke, L. Xue, F. Thiele and S. Fu. Assessment of explicit algebraic stress models in transonic flows. *Engineering Turbulence Modelling and Experiments 4, Proc. 4th Int. Symposium on engineering Turbulence Modelling and Measurements, Corsica, France*, 659–668, (1999).
- [21] S. Wallin, A. V. Johansson. An explicit algebraic Reynolds stress model for incompressible and compressible turbulent flows. *J. Fluid Mech.*, **403**, 89–132, (2000).
- [22] Ch. Gleyzes. Opération décrochage - Résultats des essais à la soufflerie F2. *RT-DERAT 55/4004 DN, ONERA*, (1988).
- [23] Ch. Gleyzes. Opération décrochage - Résultats de la 2ème campagne d’essais à F2 – Mesures de pression et vélocimétrie laser. *RT-DERAT 55/5004 DN, ONERA*, (1989).